



Embedded Young Massive Star Clusters in the Antennae Merger

Hao He¹ , Christine Wilson¹ , Nathan Brunetti¹ , Molly Finn² , Ashley Bemis³ , and Kelsey Johnson^{2,4} ¹McMaster University 1280 Main St W, Hamilton, ON, L8S 4L8, Canada; heh15@mcmaster.ca²University of Virginia, 530 McCormick Road, Charlottesville, VA 22904, US³Leiden University, Rapenburg 70, 2311 EZ, Leiden, The Netherlands

Received 2021 September 14; revised 2022 February 13; accepted 2022 February 15; published 2022 March 28

Abstract

The properties of young massive clusters (YMCs) are key to understanding the star formation mechanism in starburst systems, especially mergers. We present Atacama Large Millimeter/submillimeter Array high-resolution (~ 10 pc) continuum (100 and 345 GHz) data of YMCs in the overlap region of the Antennae galaxy. We identify six sources in the overlap region, including two sources that lie in the same giant molecular cloud (GMC). These YMCs correspond well with radio sources in lower-resolution continuum (100 and 220 GHz) images at GMC scales (~ 60 pc). We find most of these YMCs are bound clusters through virial analysis. We estimate their ages to be ~ 1 Myr and that they are either embedded or just beginning to emerge from their parent cloud. We also compare each radio source with a $\text{Pa}\beta$ source, and find they have consistent total ionizing photon numbers, which indicates they are tracing the same physical source. By comparing the free-free emission at ~ 10 pc scale and ~ 60 pc scale, we find that $\sim 50\%$ of the free-free emission in GMCs actually comes from these YMCs. This indicates that roughly half of the stars in massive GMCs are formed in bound clusters. We further explore the mass correlation between YMCs and GMCs in the Antennae and find it generally agrees with the predictions of the star cluster simulations. The most massive YMC has a stellar mass that is 1%–5% of its host GMC mass.

Unified Astronomy Thesaurus concepts: [Interstellar medium \(847\)](#); [Starburst galaxies \(1570\)](#); [Star clusters \(1567\)](#); [Star formation \(1569\)](#)

1. Introduction

How massive star clusters form is one of the major unsolved problems in star formation. Massive cluster formation was ubiquitous in the early universe, as witnessed by the populations of old massive globular clusters found in galaxies of all masses and morphologies (Harris et al. 2013). Indeed, given that the fraction of stellar mass contained in globular clusters today may be 10% or less of their initial mass as protoclusters (Fall & Zhang 2001; Whitmore et al. 2007; Li & Gnedin 2014), massive clusters should have been one of the most important modes of star formation in the early universe. In addition, current theory suggests that star formation is caused by fragmentation of hierarchically collapsing giant molecular clouds (GMCs; e.g., McKee & Ostriker 2007), which naturally leads to the conclusion that stars tend to form together in bound clusters. Both theory (Kruijssen 2012) and observations (Adamo et al. 2020) suggest that for ultra/luminous infrared galaxies (U/LIRGs), more than 50% of stars are formed in bound clusters. Therefore, studying young massive star clusters (YMCs) will help us understand the star-forming process in starburst systems.

Large populations of YMCs are seen in a diverse range of interacting galaxies and merger remnants by the Hubble Space Telescope (HST), from the M51 system (Scoville et al. 2001) to the Antennae (Whitmore et al. 1999, 2010) to Arp 220 (Scoville et al. 2000; Zhang et al. 2001). Of all the systems studied so far, the Antennae stands out for its uniquely large

population of YMCs (Scoville et al. 2000; Wilson et al. 2006) and massive molecular clouds (Wilson et al. 2003), while its proximity (22 Mpc; Schweizer et al. 2008) allows us to obtain the highest possible spatial resolution. Multiwavelength observations have mapped out the distribution of optically visible young clusters (Whitmore et al. 2010) as well as the far-infrared emission that traces buried star formation (Klaas et al. 2010). Much of the far-infrared emission is located in the overlap region (Stanford et al. 1990), a region that is also rich in molecular gas (Wilson et al. 2003; Whitmore et al. 2014; Schirm et al. 2016) and radio continuum emission (Neff & Ulvestad 2000). The overlap region also contains two bright water masers, which are a common indicator of massive star formation (Brogan et al. 2010). However, optical observations generally miss extremely young clusters (ages $< \text{few Myr}$; Johnson & Kobulnicky 2003; Johnson et al. 2004; Reines et al. 2008; Johnson et al. 2009; Hannon et al. 2019) that have high dust extinction. Whitmore et al. (2010) suggest that about 16% of star clusters in the Antennae are hidden from view in the optical. However, since radio observations are generally unaffected by dust extinction (Murphy et al. 2011), we can use radio frequencies to probe these extremely young YMCs.

In this paper, we measure YMC properties using Atacama Large Millimeter/submillimeter Array (ALMA) continuum images at ~ 10 pc scale. We compare these images with continuum images at GMC scales (~ 60 pc) to explore various correlations between the YMCs and their host GMCs. In Section 2, we describe the observations and how we processed the data. In Section 3, we describe how we measure various quantities, such as free-free flux, dust flux, temperature, and velocity dispersion. We then derive the stellar mass and gas mass based on those quantities. In Section 4, we use those quantities to explore the evolutionary stage and dynamical state of the YMCs. In Section 5, we compare various quantities,

⁴ Adjunct Astronomer at the National Radio Astronomy Observatory.



Table 1
Summary of the ALMA Continuum Observations of the Antennae

Project Code	Central Frequency (GHz)	Beam (")	Arrays Used	LAS ^a (")	rms Noise (mJy beam ⁻¹)
2018.1.00272.S	100	0.57×0.43	12m+7 m	70	0.011
2018.1.00272.S	220	0.63×0.59	12m+7 m	41	0.054
2016.1.00041.S	100	0.11×0.11	12 m	4.1	0.016
2016.1.00041.S	345	0.11×0.11	12 m	4.1	0.04

Note.

^a LAS stands for largest angular scale.

such as the star formation rate (SFR) and total mass at YMC and GMC scales, to study the correlation between these two types of objects.

2. Observations and Data Reduction

2.1. Continuum at Star Cluster Resolution

The continuum data at star cluster resolution is from ALMA project 2016.1.00041.S (PI: Christine Wilson). This project only has continuum observations from the 12 m array, and covers ALMA Bands 3 (100 GHz) and 7 (345 GHz). The total bandwidth for each spectral window is 2000 MHz. The spatial resolution for both frequency bands is about $0''.1$ (~ 10 pc). The largest angular scale is about $4''.1$ (~ 500 pc; Table 1).

The original reduction scripts were used to calibrate the raw data, using CASA version 4.7.2. All of the imaging steps were carried out using CASA version 5.1.0-70. Before imaging, we binned the channels in the calibrated measurement set to a channel width of 125 MHz for Band 3 and 250 MHz for Band 7. We then ran `tclean` on the measurement set and did the clean interactively. To match the spatial scale of the Band 3 and Band 7 images, we set the lowest `uvrange` to be $50\text{ k}\lambda$. We used a robust parameter of 0.5 for the `tclean` command. Finally, we used the CASA command `imsmooth` to smooth both images to a beam size of $0''.11 \times 0''.11$ (12 pc).

2.2. Continuum at GMC Resolution

The continuum data at GMC resolution is acquired from project 2018.1.00272.S (PI: Christine Wilson). This project has observations with both the 7 m array and 12 m extended and compact configuration arrays, and covers frequencies in ALMA Bands 3 (110 GHz) and 6 (220 GHz), with various spectral lines detected (Brunetti et al. 2022, in preparation). The total usable bandwidth for each of the spectral windows is 1875 MHz for the 12 m array and 2000 MHz for the 7 m array. The highest spectral resolution is 0.976 MHz (Table 1).

The original reduction scripts were used to calibrate the raw data, using CASA version 5.4.0-70. We used CASA 5.6.1 to image the continuum in Band 3 and Band 6, using all of the spectral windows in each band. Before imaging, we flagged the channels with detected spectral lines and combined data from different arrays into a single measurement set. We also binned the channels to a channel width of 125 MHz to speed up the imaging process. The imaging used the CASA command `tclean`, with the clean threshold set to be two times the rms noise. We chose the `specmode` to be “mfs” and the masking method to be “auto-multithresh” (Kepley et al. 2020), to choose the clean regions automatically. The “auto-multithresh”

parameters were left as the default values. We applied primary beam correction to the cleaned images.

2.3. CO Line Data at GMC Resolution

The $^{12}\text{CO } J=2-1$ data with GMC resolution is also from project 2018.1.00272.S (PI: Christine Wilson). The image cube was made with a modified version of the PHANGS pipeline (Leroy et al. 2021, and see the details in N. Brunetti et al. 2022, in preparation). The beam size was rounded to $0''.51 \times 0''.51$ (54 pc). The velocity resolution is 2.65 km s^{-1} . The rms is 2.6 K.

2.4. CO Line Data at Star Cluster Resolution

The $^{12}\text{CO } J=2-1$ data with star cluster resolution is from Finn et al. (2019). The beam size of the data is $0''.12 \times 0''.09$ (13 pc). The channel width of the cube is 5 km s^{-1} . The rms of the cube is 1.2 mJy beam^{-1} .

2.5. HST Data

We use the $\text{Pa}\beta$ and I -band maps from Whitmore et al. (2014) for comparison with the radio continuum. Both images have a resolution of $\sim 0''.2$. The I -band image has a pixel size of $0''.04$, while the $\text{Pa}\beta$ image has a larger pixel size of $0''.128$. In Section 4.4, we use $\text{Pa}\beta$ to calculate the total ionized photon number ($Q(H^0)$), and compare it with that derived from the 100 GHz continuum.

For $\text{Pa}\beta$, we perform continuum subtraction using the HST J -band image. Since the wavelengths of the two filters are close to each other, we adopt a simple model, where the intensity at the J band for background stars is the scaled version of that in the $\text{Pa}\beta$ image. Therefore, the $\text{Pa}\beta$ intensity is

$$I_{\text{Pa}\beta} = I_{\text{F128N}} - \beta \cdot I_{\text{F116W}}, \quad (1)$$

where I_{F128N} is the $\text{Pa}\beta$ intensity before continuum subtraction, I_{F116W} is the J -band intensity, and $I_{\text{Pa}\beta}$ is the intensity after continuum subtraction. To calculate the β , we draw apertures around sources that are pointlike and not associated with any galaxy structures, which are likely background stars. We then measure the fluxes of these sources from the F128N and F116W filters. We also measure the background fluxes by drawing apertures close to these background stars. We then plot the background-subtracted fluxes from the two filters and fit a proportional relation to get β . We calculate $\beta = 0.03$, which is close to the β value in Kessler et al. (2020). We then reproject the J -band image to the $\text{Pa}\beta$, and apply Equation (1) to perform the continuum subtraction.

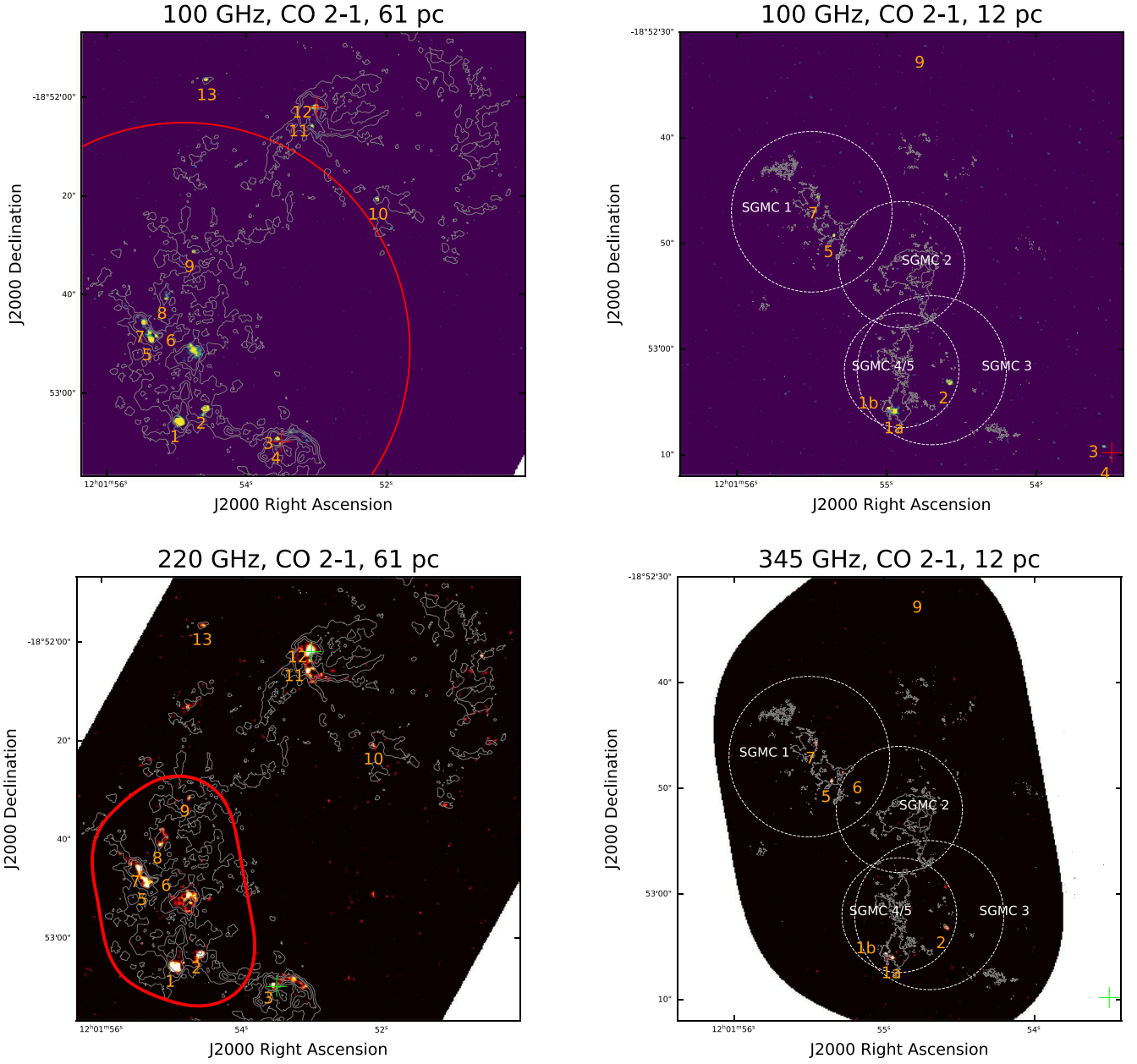


Figure 1. Continuum image of the Antennae at (upper) 100 GHz, (lower left) 230 GHz, and (lower right) 340 GHz. The continuum images in the left panels are from ALMA project 2018.1.00272.S, with a physical resolution of 61 pc. The contours are from the $^{12}\text{CO } J = 2-1$ moment 0 map from N. Brunetti et al. (2022, in preparation). The red apertures show the field of view of the high-resolution images shown in the right panels. The continuum images in the right panels are from ALMA project 2016.1.00041.S, with a physical resolution of 12 pc. The contours in the right panels are from the $^{12}\text{CO } J = 2-1$ moment 0 map from Finn et al. (2019). The dashed circles in the right panels show the locations of the super giant molecular clouds (SGMCs) identified in Wilson et al. (2000), with diameters equal to those of the SGMCs. The red and green plus signs show the locations of two nuclei from Zhang et al. (2001).

3. Measurements and Derived Quantities

3.1. Source Identification

The continuum images from the two ALMA continuum projects are shown in Figure 1. As we can see, the continuum images at GMC resolution have higher sensitivity. Therefore, we use the 100 GHz GMC-resolution map, which has the highest sensitivity among all the continuum data, as a guide for finding sources in the higher-resolution maps by eye. The identified sources are labeled in Figure 1. As we can see, there are ~ 10 continuum sources that are likely to be YMCs. The reason that we do not observe as many radio continuum sources as optical clusters is mainly due to the limited sensitivity of the

radio data. As mentioned in Section 2, a continuum point source with a signal-to-noise ratio (S/N) of 5 corresponds to a $7.2 \times 10^5 M_{\odot}$, which is greater than the masses of most star clusters in spiral galaxies. On the other hand, the lifetimes of the radio clusters are also much lower than those of the optical clusters (see Section 4.1 for a detailed discussion), which also contributes to the limited number of sources we detected.

We then match the 100 GHz low-resolution image with the high-resolution image to check if the continuum source is still pointlike in the high-resolution image. Source 8 is not detected in the high-resolution image, and may be dominated by GMC-scale emission that is filtered out in the high-resolution image. Another interesting source is source 1, which is the brightest

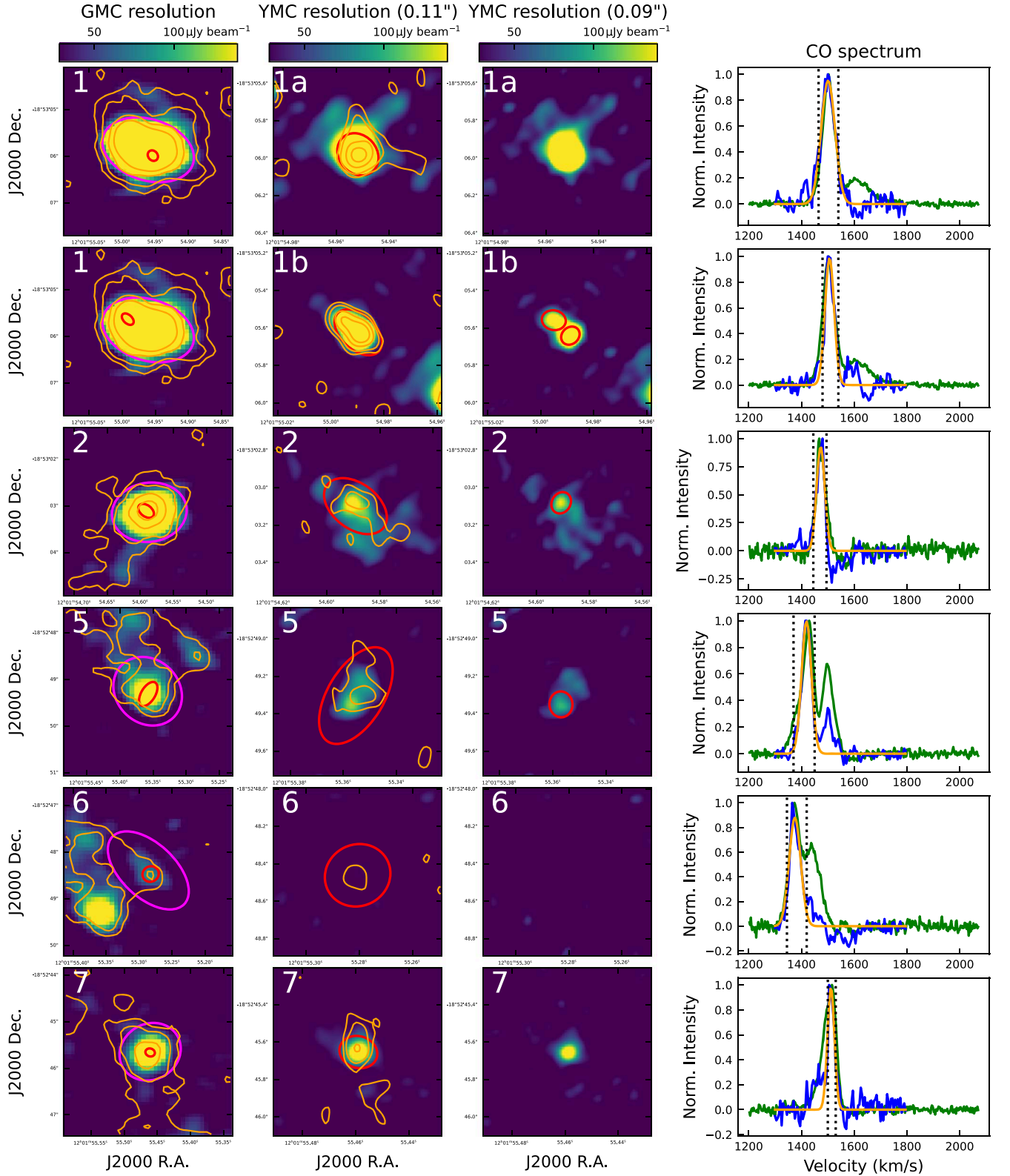


Figure 2. Continuum images (left) and $^{12}\text{CO } J=2-1$ spectra (right) of individual YMCs. For the images, the left column shows the 100 GHz data at GMC resolution (61 pc). The orange contours are the 220 GHz data at similar resolution. The magenta apertures are the apertures used to measure the flux at GMC scales. The red apertures are the apertures used to measure the flux at YMC scales. The middle and right columns show the 100 GHz data at YMC scales with slightly different resolutions. The orange contours in the middle column are the 345 GHz data at the same resolution. The red apertures in the right column are the fitted Gaussian beams for the substructures in some of the YMCs. The $^{12}\text{CO } J=2-1$ spectra are normalized to the peak of the line emission measured in the magenta apertures in the left column (green spectrum) and the red apertures in the middle column (blue spectrum). The orange curves are the fitted Gaussian function to the measured spectrum (shown in blue). The vertical dotted lines specify the velocity ranges that we use to fit the Gaussian spectra.

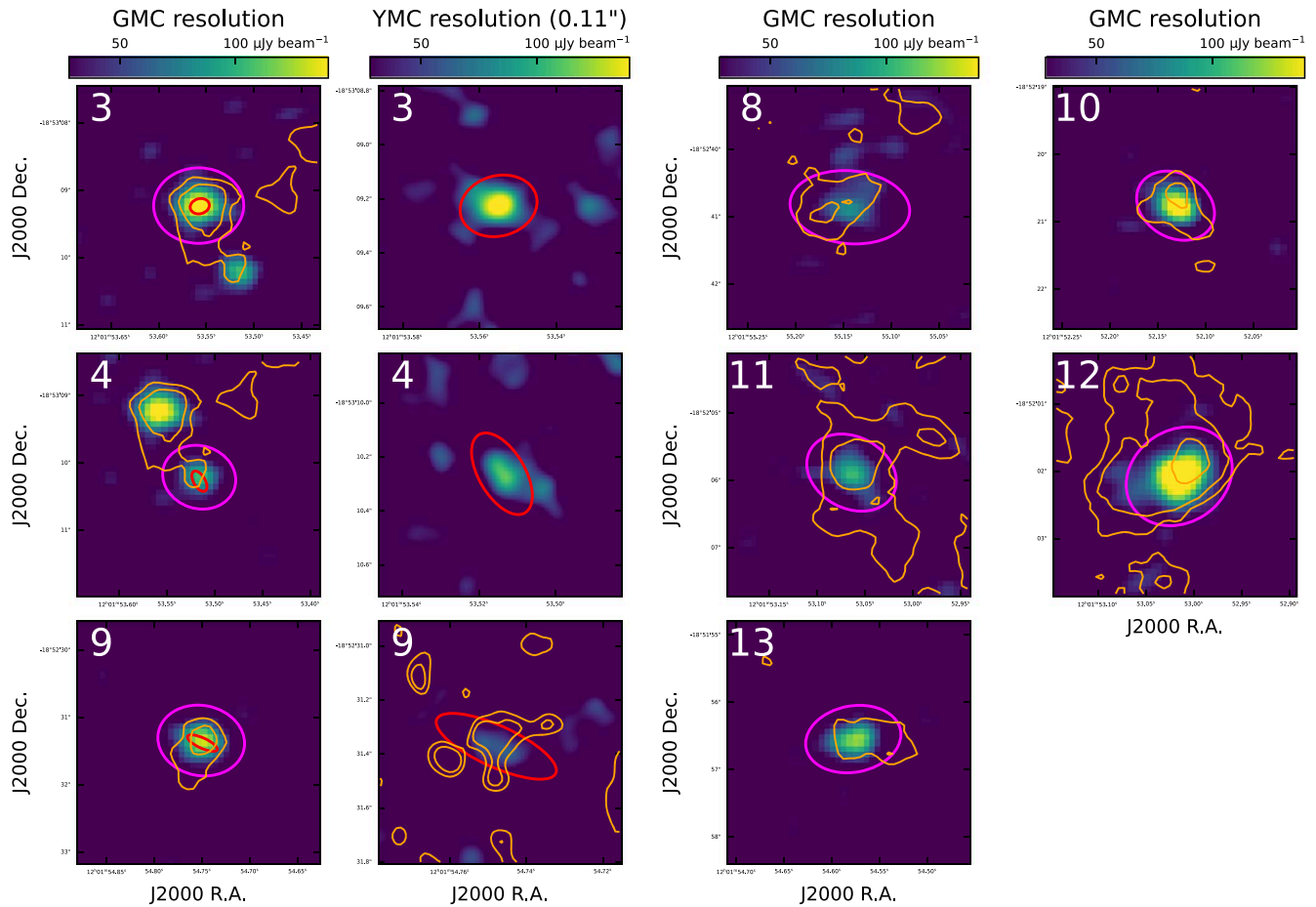


Figure 3. Images for YMCs that do not have $^{12}\text{CO } J=2-1$ observations at 12 pc scale. Left: the three sources that have 100 GHz images at YMC scale. Right: the remaining sources that only have 100 GHz GMC-resolution data. The orange contours in the GMC-resolution images are the 220 GHz continuum and those in the YMC-resolution images are the 345 GHz continuum. The magenta apertures are used to measure the GMC fluxes, while the red apertures are used to measure the YMC fluxes.

source in the continuum map. This separates into two sources in the higher-resolution image. Furthermore, source 1b further divides into two subsources in our highest-resolution image, as shown in Figure 2. We can see that sources 1a and 1b have similar velocities (Figure 2). This comparison suggests that these two clusters are close to each other in 3D space and are probably interacting with each other within a single GMC. Multiple YMCs within a single GMC have also been observed in NGC 253 (Leroy et al. 2015, 2018). Statistical studies (e.g., Grasha et al. 2018; Tsuge et al. 2019) also show that a significant fraction of GMCs will form more than one YMC.

We further check the 220 GHz continuum image at GMC scale and the 345 GHz continuum image at star cluster scale. An interesting source is source 6, which is not seen in the 100 GHz continuum image at ~ 10 pc scale, but is seen in both the 220 and 345 GHz continua. Since the 100 GHz continuum traces free-free emission from extremely young stars, it seems likely that this source is dominated by a clump of gas with stars yet to form.

Sources 1a, 1b, 2, 5, 6, and 7 have all been covered by high-resolution observations of 100 and 345 GHz continua and the $^{12}\text{CO } J=2-1$ line with high-S/N detections. Therefore, we will focus on these sources in the rest of this paper. Images for these sources are shown in Figure 2, while the remaining sources are shown in Figure 3. The measured properties of all

sources are listed in Tables 2 and 3. The comparison between the radio continuum and $\text{Pa}\beta$ is shown in Figure 4.

3.2. Size, Flux, and Line Width Measurements

We determine the sizes of the YMCs using the CASA task `imfit` on the high-resolution 100 GHz data. This task fits a 2D Gaussian function for a selected encircled region. First, we draw an elliptical aperture around each identified source by eye. We then run the task `imfit` to get the major axis, minor axis, and position angle of the fitted beam. We confirm the fitting results by comparing the half-maximum contour of the source with the fitted apertures on the map. The `imfit` command also gives us the Gaussian size deconvolved from the beam, which tells us the true source size. We list the major axes of the deconvolved Gaussians in Table 2. For source 6, since we do not have a detection in the 100 GHz continuum, we use the 345 GHz continuum image to fit the source. Note that the beam size of 12 pc is larger than most YMCs in the literature, which have measured sizes of about 2 pc (Leroy et al. 2018). If the YMCs in the Antennae were to have a similar size, we would expect our derived sizes to be upper limits to the true source size.

We use an aperture with a diameter equal to two times the fitted Gaussian FWHM to measure the flux. The flux

Table 2
Measured Quantities of YMCs in the Antennae

Index (1)	Coordinates (J2000) (2)	$S_{100\text{GHz}}$ (mJy) (3)	$S_{340\text{ GHz,dust}}$ (mJy) (4)	σ_v (km s $^{-1}$) (5)	T_{kin} (K) (6)	d_{FWHM} (arcsec) (7)
1a	12 ^h 01 ^m 54 ^s .95, -18 ^d 53 ^m 05 ^s .98	1.2 ± 0.04	<0.04	<26 ± 1	40 ± 2	0.085 ± 0.01
1b	12 ^h 01 ^m 54 ^s .99, -18 ^d 53 ^m 05 ^s .62	0.69 ± 0.04	0.89 ± 0.1	<19 ± 1	53 ± 2	0.12 ± 0.02
2	12 ^h 01 ^m 54 ^s .59, -18 ^d 53 ^m 03 ^s .10	0.41 ± 0.05	0.33 ± 0.1	<17 ± 2	42 ± 2	0.17 ± 0.04
3	12 ^h 01 ^m 53 ^s .55, -18 ^d 53 ^m 09 ^s .23	0.28 ± 0.07	0.12 ± 0.03
4	12 ^h 01 ^m 53 ^s .51, -18 ^d 53 ^m 10 ^s .26	0.19 ± 0.07	0.14 ± 0.05
5	12 ^h 01 ^m 53 ^s .51, -18 ^d 53 ^m 10 ^s .26	0.37 ± 0.07	0.67 ± 0.1	<19 ± 1	48 ± 2	0.28 ± 0.06
6	12 ^h 01 ^m 55 ^s .28, -18 ^d 52 ^m 48 ^s .46	<0.081	0.32 ± 0.1	<23 ± 2	48 ± 2	0.14 ± 0.03
7	12 ^h 01 ^m 55 ^s .46, -18 ^d 52 ^m 45 ^s .65	0.23 ± 0.03	0.25 ± 0.07	<15 ± 1	38 ± 2	0.06 ± 0.02
9	12 ^h 01 ^m 54 ^s .75, -18 ^d 52 ^m 31 ^s .37	0.14 ± 0.06	0.19 ± 0.2	0.22 ± 0.09

Note. (1) Source ID. (2) Coordinates. (3) Flux at 100 GHz. (4) Estimated dust flux at 345 GHz. (5) $^{12}\text{CO } J=2-1$ velocity dispersion. All values are upper limits (see Section 3.2). (6) Kinetic temperature from LTE analysis. (7) Deconvolved FWHM of the source from CASA task `imfit`. At the distance of the Antennae (22 Mpc), $0.1'' = 10.67$ pc.

Table 3
Derived Physical Properties of YMCs

Index (1)	$\log_{10} M_*$ (M_\odot) (2)	$\log_{10} M_{\text{gas}}$ (M_\odot) (3)	$\log_{10} M_{\text{vir}}$ (M_\odot) (4)	$\log_{10} \Sigma_{\text{tot}}$ ($M_\odot \text{ pc}^{-2}$) (5)	R_h (pc) (6)	A_V (10^2 mag) (7)
1a	6.2 ± 0.01	<5.4	<6.8 ± 0.06	4.4 ± 0.2	4.5 ± 0.5	< 2
1b	6.0 ± 0.03	6.8 ± 0.05	<6.7 ± 0.09	4.7 ± 0.2	6.4 ± 1.1	22 ± 8
2	5.8 ± 0.05	6.4 ± 0.15	<6.8 ± 0.13	4.1 ± 0.2	9.1 ± 2.1	4.5 ± 2.6
5	5.7 ± 0.08	6.7 ± 0.08	<7.0 ± 0.1	3.9 ± 0.2	15 ± 3	3.2 ± 1.5
6	<5.1	6.3 ± 0.15	<6.9 ± 0.1	4.1 ± 0.2	7.5 ± 1.6	6.1 ± 3.3
7	5.5 ± 0.05	6.3 ± 0.13	<6.3 ± 0.2	4.7 ± 0.3	3.2 ± 1.1	28 ± 20

Note. (1) Source ID. (2) Stellar mass. (3) Dust mass. (3) Gas mass derived from dust continuum (see Section 3.5). (4) Virial mass as upper limit. (5) Total surface density (gas+star) of YMCs. (6) Half-light radius. (7) Optical extinction at the V band.

uncertainty is calculated as

$$Err = \text{RMS} \times \sqrt{N_{\text{beam}}} / \text{pbcor},$$

where rms is the image noise, N_{beam} is the number of beams in the aperture, and pbcor is the value for the primary beam response.

We also measure the line widths for the star clusters using the $^{12}\text{CO } J=2-1$ map from Finn et al. (2019) and the same apertures used for the flux measurements. We export the spectrum for each source and then fit a Gaussian to get the velocity dispersion. Many spectra show an extra bump besides the major peak, which comes from gas outside the star cluster. Therefore, we manually set the upper and lower limits for the fitting range to only fit the Gaussian to the major peak. The fits are shown in Figure 2. In addition, we apply the same method to draw the apertures on the sources in the 100 GHz GMC map (see Section 5.1). We also overlay the GMC-scale $^{12}\text{CO } J=2-1$ spectrum measured in those apertures in the right column of Figure 2. As we can see, the velocity dispersions at YMC scale are almost the same as those at GMC scale. We suspect that this is because the velocity dispersion as measured with $^{12}\text{CO } J=2-1$ at YMC scale still traces the overall cloud motions. In this case, the measured velocity dispersion for YMC should be treated as the upper limit.

3.3. Separating Dust Emission and Free-Free Emission

At 345 GHz, dust emission is usually expected to be dominant. However, there is still a significant fraction of

free-free emission at this frequency for these YMCs. To calculate the dust mass, we need to separate the dust emission from the free-free emission. To begin with, we assume that free-free emission dominates the total emission at 100 GHz. This assumption has been shown to hold for YMCs in the Henize 2–10 dwarf galaxy with a similar resolution of ~ 10 pc (Costa et al. 2021). Free-free emission scales with frequency as a power-law function with an index of -0.1 (Ginsburg et al. 2016). Therefore, we can predict the free-free flux at 340 GHz using

$$S_{345\text{GHz,ff}} = S_{100\text{GHz}} \left(\frac{345 \text{ GHz}}{100 \text{ GHz}} \right)^{-0.1}, \quad (2)$$

where $S_{100\text{GHz}}$ is the continuum flux at 100 GHz. Then the dust flux is just

$$S_{345\text{GHz,dust}} = S_{345\text{GHz}} - S_{345\text{GHz,ff}}. \quad (3)$$

We will use the dust-only flux to calculate the dust and gas mass in the YMCs.

3.4. Gas Temperature

To calculate the dust mass from the dust flux, we need to assume a dust temperature. We assume that the dust temperature is equal to the gas kinetic temperature. The gas temperature can then be constrained through the $^{12}\text{CO } J=2-1$ observations (Finn et al. 2019), by assuming the local thermal equilibrium (LTE). The basic formula to connect the peak

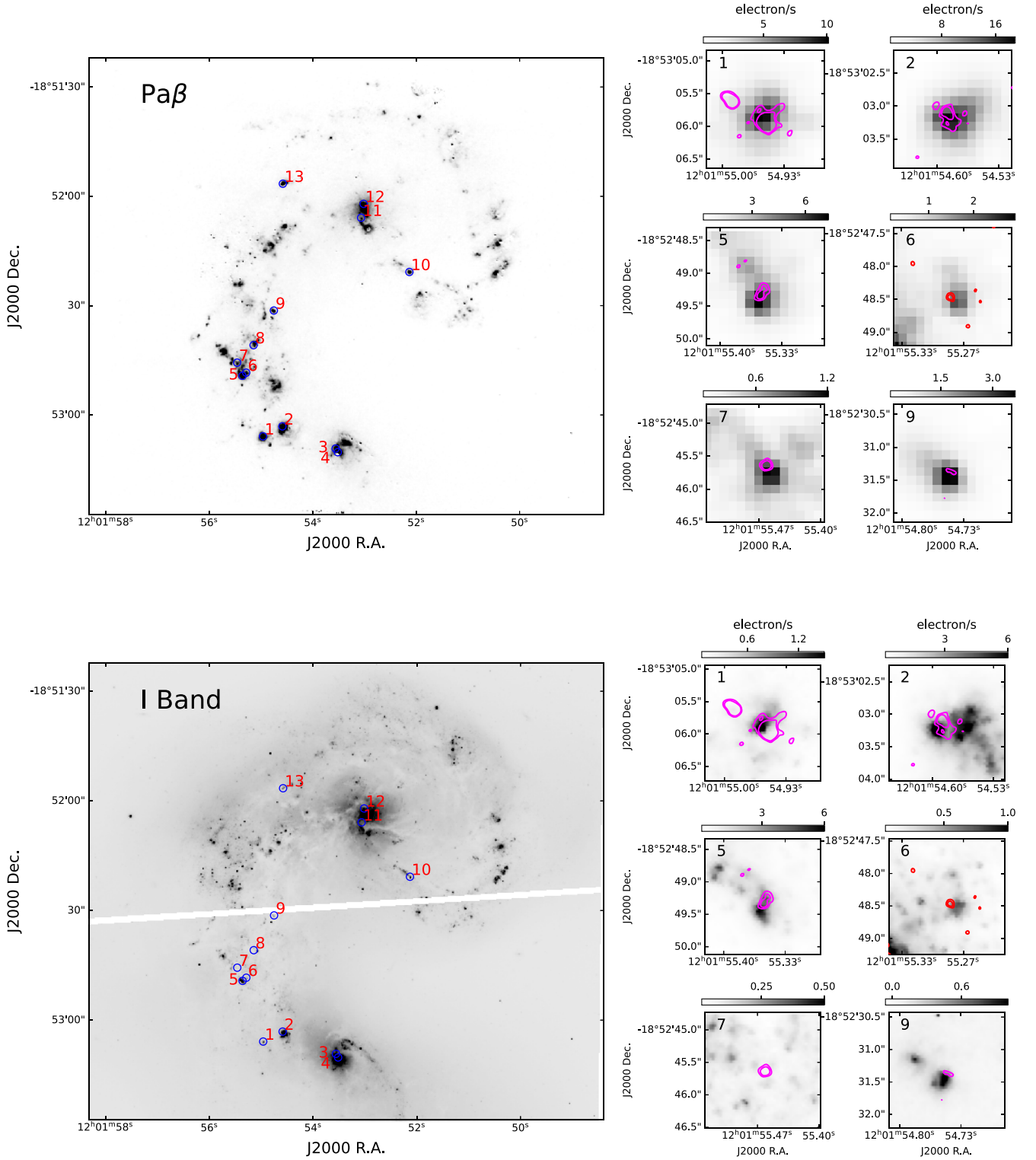


Figure 4. The Paschen β (upper) and I -band (lower) maps of the Antennae. Upper left: the Paschen β map of the Antennae (Whitmore et al. 2014), with the positions of the radio continuum sources labeled as blue circles. Upper right: zoom-in $\text{Pa}\beta$ images for the individual YMCs. The magenta and red contours are the 100 and 345 GHz continua at 12 pc resolution. The typical offset between the $\text{Pa}\beta$ and radio continuum sources is ~ 11 pc. Lower left: the HST I -band image for the entire field of view of the Antennae. Lower right: zoom-in I -band images for each YMC.

brightness temperature and the gas temperature is

$$T_b = \left[\frac{h\nu/k}{\exp(h\nu/kT_{\text{ex}}) - 1} - \frac{h\nu/k}{\exp(h\nu/kT_{\text{bg}}) - 1} \right] (1 - e^{-\tau}), \quad (4)$$

where T_b is the peak brightness temperature, T_{ex} is the excitation temperature, $T_{\text{bg}} = 2.73\text{K}$ is the background temperature, ν is the observed frequency of the line, τ is the optical depth, h is Planck's constant, and k is the Boltzmann constant. For $^{12}\text{CO } J=2-1$, $h\nu/k = 11.07$ K. We also assume $\tau \rightarrow \infty$.

Table 4
Corresponding Optical YMCs

Index	Region	HST ID	$\log_{10} M_*$ (M_\odot)	Age (Myr)	A_V (mag)	$S_{\text{Pa}\beta}$ ($10^{-14} \text{ erg s}^{-1}$)	$S_{100\text{GHz,smooth}}$ (mJy)	Cross ID
(1)	(2)	(3)	(4)	(5)	(6)	(7)	(8)	(9)
1a	SGMC 4/5	14612	6.8	1.0	7.3	1.92	2.1 ± 0.05	B1
2	SGMC 4/5	15492	6.6	2.5	3.0	4.1	1.3 ± 0.07	B
5	SGMC 1	19330	5.5	1.0	1.0	0.84	0.4 ± 0.04	D
6	SGMC 1	19807	...	8	5.0	0.24	<0.075	D1
7	SGMC 1	3.5	4.1	0.16	0.61 ± 0.05	D2
9	LT	3475	6.0	1.0	4.2	0.36	0.35 ± 0.07	E3

Note. (1) Source ID from Table 2. (2) Region defined in Whitmore et al. (2014), based on the $^{12}\text{CO } J=3-2$ map. (3) HST ID for the star clusters identified in Whitmore et al. (2010; sources 1a, 2, 5, 6) or Whitmore & Zhang (2002; source 9). (4) Stellar mass of the star clusters from Whitmore et al. (2010) or Whitmore & Zhang (2002). (5) Age of the star clusters from Whitmore et al. (2014). (6) Extinction at V band from Whitmore et al. (2014). (7) The flux measured for Pa β sources. (8) The flux measured for the 100 GHz radio sources smoothed to the resolution of $0.201''$. (9) Cross ID of the K-band sources identified in Gilbert & Graham (2007).

Applying all these assumptions, we can express T_{kin} as

$$T_{\text{kin}} = T_{\text{ex}} = \frac{11.07}{\ln \left[1 + \frac{11.07}{T_b + 0.195} \right]}. \quad (5)$$

The gas temperatures are shown in Table 2. We see that almost all the sources have $T_{\text{kin}} \sim 40$ K. Rico-Villas et al. (2020) show that the YMCs in NGC 253 have temperatures of 150–300 K, based on line ratios of HC_3N . We note that our physical beam size (12 pc) is much larger than those for NGC 253 (1.9 pc). As discussed in Section 4.1, we probably overestimate the sizes of these YMCs. Therefore, our apertures probably include a large fraction of surrounding gas with lower temperatures.

3.5. Gas Mass

The gas mass is calculated from the dust emission after correcting for free-free contamination. We calculate the dust mass based on the equation in Wilson et al. (2008):

$$M_{\text{dust}} = 74, 220 S_{880} D^2 \frac{(e^{17/T} - 1)}{\kappa} (M_\odot), \quad (6)$$

where S_{880} is the flux from dust emission at $880 \mu\text{m}$ (345 GHz), D is the distance in Mpc, T is the dust temperature in Kelvin, and κ is the dust emissivity in $\text{cm}^2 \text{g}^{-1}$. In this case, we assume $\kappa = 0.9 \text{ cm}^2 \text{g}^{-1}$ (Wilson et al. 2008). The dust mass is highly dependent on the dust temperature. We assume the dust temperature is equal to the gas kinetic temperature (see Section 3.4).

From the dust mass, we then calculate the molecular gas mass based on the gas-to-dust mass ratio:

$$M_{\text{gas}} = \frac{[\text{Gas}]}{[\text{Dust}]} \times M_{\text{dust}}. \quad (7)$$

We adopt a gas-to-dust mass ratio of 120 from Wilson et al. (2008). The gas masses are given in Table 3.

3.6. Extinction

From the gas mass that we calculate, we can then derive the gas surface density, which is directly related to the optical extinction A_V . We can compare A_V from the dust emission with that from the optical data to see if they agree with each other. We adapt the equation in Draine (2003) to calculate the visual

extinction A_V from the gas surface density:

$$A_V = 0.0491 \Sigma_{\text{gas, YMC}}, \quad (8)$$

where $\Sigma_{\text{gas, YMC}}$ is the YMC gas surface density derived from the dust continuum flux and deconvolved radius in $M_\odot \text{pc}^{-2}$. The A_V values (Table 3) show that these sources generally have visual extinctions of hundreds of magnitudes. These extinctions are much larger than the A_V values derived for the optical counterparts of these YMCs (Table 4). We will discuss this discrepancy in Section 4.4.

3.7. Total Ionizing Photon Number

We can use both the 100 GHz continuum and the Pa β line to calculate the total number of ionizing photons, $Q(H^0)$, since they both trace emission from the ionized gas. We compare the $Q(H^0)$ from two different data sets in Section 4.4. $Q(H^0)$ can also be used to calculate the stellar mass of young star clusters, based on a few assumptions.

For the 100 GHz continuum, we assume the emission is dominated by free-free emission. Therefore, we can calculate the total number of ionizing photons using the equation from Murphy et al. (2011):

$$\left[\frac{Q(H^0)}{\text{s}^{-1}} \right] = 6.3 \times 10^{25} \left(\frac{T_e}{10^4 \text{ K}} \right)^{-0.45} \left(\frac{\nu}{\text{GHz}} \right)^{0.1} \times \left(\frac{L_\nu^{\text{T}}}{\text{erg s}^{-1} \text{Hz}^{-1}} \right), \quad (9)$$

where $Q(H^0)$ is the total number of ionizing photons, T_e is the temperature of the H II region (generally 10^4 K), $\nu = 100$ GHz is the observed frequency, and L_ν^{T} is the luminosity of the free-free emission at the observed frequency.

For the Pa β data, we use the equation to calculate $Q(H^0)$ from H α (Murphy et al. 2011). Assuming $\text{H}\alpha/\text{Pa}\beta = 17.6$ (Case B recombination, $T = 10^4$ K, and $n_e = 10^4 \text{ cm}^{-3}$; given by Osterbrock 1989; Cleri et al 2020), the equation to calculate $Q(H^0)$ from Pa β is given by

$$Q_{\text{Pa}\beta}(H^0) = 1.3 \times 10^{13} 10^{0.4 A_{\text{Pa}\beta}} L_{\text{Pa}\beta}. \quad (10)$$

where $L_{\text{Pa}\beta}$ is the luminosity of Pa β in erg s^{-1} and $A_{\text{Pa}\beta}$ is the extinction for the Pa β line in magnitude. $A_{\text{Pa}\beta}$ can be derived from A_V , based on the extinction curve in Calzetti et al. (2000),

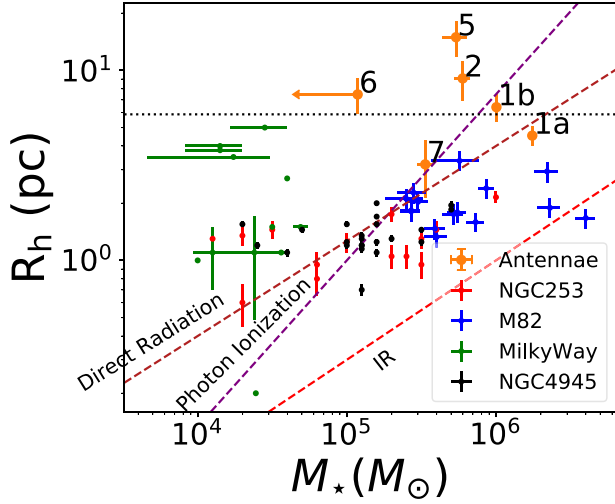


Figure 5. The half-light radius vs. stellar mass for YMCs in the Antennae, NGC 253 (Leroy et al. 2018), M82 (McCrady & Graham 2007), Milky Way (Krumholz et al. 2019), and NGC 4945 (Emig et al. 2020). The horizontal dotted line marks our YMC resolution ($0''.11$). The diagonal dashed lines specify the area where the feedback from direct radiation (brown), photoionization (purple), and IR radiation (red) is effective for dispersing the surrounding gas (Krumholz et al. 2019). For direct radiation and photoionization, the effective area is leftward, and for IR radiation, the effective area is rightward.

as

$$A_{\text{Pa}\beta} = A_V \times \frac{k_{\text{P}\beta}}{k_V} = 0.43A_V, \quad (11)$$

where $k_{\text{P}\beta}$ and k_V are the values of the reddening curve at the two wavelengths (Calzetti et al. 2000, Equation (4)).

3.8. Stellar Mass

From $Q(H^0)$, we can calculate the stellar mass using the equation from Leroy et al. (2018):

$$M_* = \frac{Q(H^0)}{4 \times 10^{46}} M_\odot. \quad (12)$$

This equation assumes a Kroupa initial mass function with a maximum stellar mass of $100 M_\odot$, and it also assumes that the YMCs have a single stellar population (SSP). The stellar masses calculated from the 100 GHz fluxes in Table 2 are given in Table 3.

4. Star Cluster Properties

4.1. Ages of the YMCs

We can estimate the ages of the YMCs by comparing the number of clusters at optical wavelengths with the number observed in the radio. This method has previously been used for estimating the ages of the YMCs in the dwarf galaxy Henize 2–10 (Kobulnicky & Johnson 1999; Johnson & Kobulnicky 2003). The number ratio is roughly the age ratio of the two populations if we assume a constant SFR during this time period. Zhang et al. (2001) estimate that there are about 1600 clusters with ages smaller than 16 Myr and masses greater than $10^4 M_\odot$. For our 100 GHz GMC map, the S/N = 5 cutoff is $\sim 7.2 \times 10^4 M_\odot$. To estimate the number of optical clusters with masses greater than that value, we assume the cluster mass

function has a slope of -2 (Krumholz et al. 2019). In this case, we expect about 200 optical clusters with masses greater than $7.2 \times 10^4 M_\odot$ and ages less than 16 Myr. Our actual 100 GHz GMC map reveals 17 continuum sources greater than that value. Based on that number, we would expect the ages of these radio YMCs to be ~ 1 Myr. Various HST studies of YMCs have adopted similar statistical counting methods, and find that the time for star clusters to dissociate from their host GMCs is about 2–3 Myr (Hollyhead et al. 2015; Grasha et al. 2018; Hannon et al. 2019). If this timescale is also true for the Antennae, we would expect that feedback has not been effective for most of our radio sources. Therefore, they should still be forming stars.

4.2. Size–Mass Relation

We plot our measurements of the YMCs in the size–mass relation, along with literature data from other galaxies (Figure 5). According to Leroy et al. (2018) and Levy et al. (2021), very young YMCs are generally very compact, with radii of 1–2 pc. However, from the fit to the size–mass relation in the LEGUS sample (Brown & Gnedin 2021), we would expect a radius of ~ 5 pc for a YMC with a stellar mass of $10^6 M_\odot$. This radius is consistent with what we measured for some of the YMCs in the Antennae. Note that the Brown & Gnedin (2021) relation for young star clusters does not extend to $10^6 M_\odot$.

We also plot dashed lines from Krumholz et al. (2019) to show the regions where feedback is effective. As we can see, most of the YMCs lie in the area where direct radiation or photoionization feedback is effective. This suggests two possibilities. One is that feedback is actually effective for these YMCs. As shown in Table 3, most YMCs, except for source 1a, have gas fractions greater than 50%. According to various observations (Whitmore & Zhang 2002; Whitmore et al. 2014; Hannon et al. 2019; Chevance et al. 2020), the timescale for feedback to disperse the gas is around 1–3 Myr. As we have calculated, these YMCs should generally have ages of ~ 1 Myr. Therefore, although feedback is expected to play a role, it has not cleared all the gas surrounding the YMCs.

On the other hand, we might overestimate the sizes of these YMCs. As shown in Figure 5, our resolution limit is higher than most of the YMCs with similar masses. As an example, suppose that the radii are overestimated by a factor of 4: cluster 1a would then fall on the line for IR radiation feedback to be effective, while the rest of the clusters would lie in the region where no feedback is effective. However, we note that the feedback region in the size–mass diagram is one projection of a complex process. In Levy et al. (2021), they find outflows in YMCs that they do not expect to be experiencing feedback, given their location in the size–mass diagram.

4.3. Virial Mass

We use the equation in Bolatto et al. (2013) to calculate the virial mass:

$$M_{\text{vir}} = 1061 R_h \sigma_v^2, \quad (13)$$

where M_{vir} is the virial mass in M_\odot , R_h is the deconvolved half-light radius in parsecs, and σ_v is the measured velocity dispersion in kilometers per second of the source. This equation assumes uniform density.

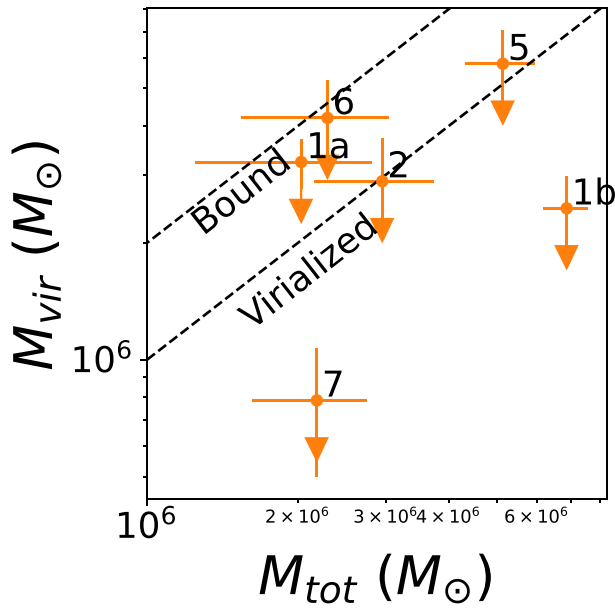


Figure 6. The comparison between the total mass and the virial mass. The two diagonal dashed lines mark the boundaries below which systems are bound or virialized. The offset between the dashed lines is a factor of 2. We can see that most of the sources are bound systems.

Figure 6 shows the comparison between virial mass and total mass. We can see that the virial masses for all the YMCs are smaller than $2 \times M_{\text{tot}}$, which implies that these YMCs are likely gravitationally bound systems.

We need to note that the virial masses of the YMCs should be treated as upper limits, because our measured velocity dispersion is tracing the overall cloud motion instead of the dispersion inside the YMC. This further confirms that all these sources should be gravitationally bound systems, and may be virialized.

Although these YMC+gas systems are currently gravitationally bound, whether the final star cluster will be gravitationally bound or not depends on the fraction of the gas mass that is eventually turned into stars. Thus, the boundedness of these very young embedded YMCs is not necessarily inconsistent with the results from Matthews et al. (2018), who found that only a small fraction of the optically visible young star clusters in the Antennae are likely to remain gravitationally bound.

4.4. Comparison with Optical Data

Based on the multiwavelength comparison in Whitmore et al. (2014), we can see that most of our sources have optical counterparts. The properties of these optical YMCs are summarized in Table 4. As we mentioned in Section 3.6, the A_V derived from the optical data is ~ 100 times smaller than that derived from the dust continuum. This difference suggests that the optical source and the radio source might just happen to be along the same line of sight. Furthermore, the radio continuum data used in Whitmore et al. (2014) only have a resolution of $\sim 0.5''$. With our new data, we can make a more precise comparison of the coordinates of the optical and radio sources. We use Pa β for this comparison, since both the 100 GHz radio continuum and Pa β trace emission from the ionized gas.

The Pa β and I -band maps for the Antennae and the individual sources are shown in Figure 4. As we can see, the Pa β image looks quite similar to the I -band image. The individual I -band sources and Pa β sources also match and have consistent offsets from the radio sources, except for source 7, which does not have I -band detection, which we hypothesize is due to extinction. To make a more quantitative comparison between the coordinates of the radio sources and those of the HST sources, we apply `imfit` on the Pa β sources to get the central coordinates, and compare them with those derived from the radio continuum. The offsets between the two central coordinates are shown in the left panel of Figure 7. As we can see, these offsets are not in a consistent direction, and so we cannot shift the coordinates of the Pa β image to align the peak of the Pa β sources with the radio sources. The offsets are generally larger than $0''.1$, which translates to a physical distance of 11 pc. In comparison, the offset between the 100 GHz and 345 GHz images are typically less than $0''.03$.

On the other hand, as mentioned in Section 3.7, we can use both images to calculate $Q(H^0)$. If the $Q(H^0)$ from the two sets of data agree with each other, then it seems likely that the Pa β emission and 100 GHz continuum are from the same physical source, instead of from two sources that happen to lie along the same line of sight. We smooth the radio continuum image to a resolution of $0''.21$, to match the Pa β image, and then use Equations (9) and (10) to calculate the total number of ionizing photons from the 100 GHz radio continuum and Pa β . As shown in the right panel of Figure 7, the total numbers of ionizing photons derived from the two data sets generally agree with each other within a factor of 2. This agreement suggests that the radio continuum and Pa β might actually trace the same physical source, despite the offsets in their coordinates.

One possible explanation is that the clumpiness or density gradients in the surrounding molecular cloud allow photons from the YMC to leak out of the cloud and ionize the surrounding HI gas (Figure 8). This has been proposed as the “blister” model (Israel 1978), to explain the spatial and velocity offsets between CO clouds and H II regions in the Milky Way. In this case, high extinction inside the cloud could prevent us from observing the Pa beta emission produced there, while the relatively low sensitivity of the radio continuum data could prevent us from detecting radio continuum emission from the H II region outside the cloud. It would explain the spatial offsets between the peaks at different wavelengths, and also why we have different A_V values from the optical data and the 345 GHz dust emission.

For source 6, the ionizing photon counts from Pa β are much higher than the upper limit derived from the 100 GHz radio continuum image. A possible scenario is that this source has already emerged from the cloud and heats the nearby GMC without ionizing much of the cloud. In this scenario, the detected 345 GHz continuum emission comes primarily from heated dust from the edge of the GMC, while any radio continuum emission from the ionized gas seen in Pa β is too faint to be detected. Another interesting object is source 7, which has lower $Q(H^0)$ derived from the Pa β emission than source 6, but which is detected in the 100 GHz continuum. Since this source does not have I -band detection, we suspect that this source is still quite embedded in the parent cloud, and only has a small amount of ionizing photons leaking out to generate the Pa β emission.

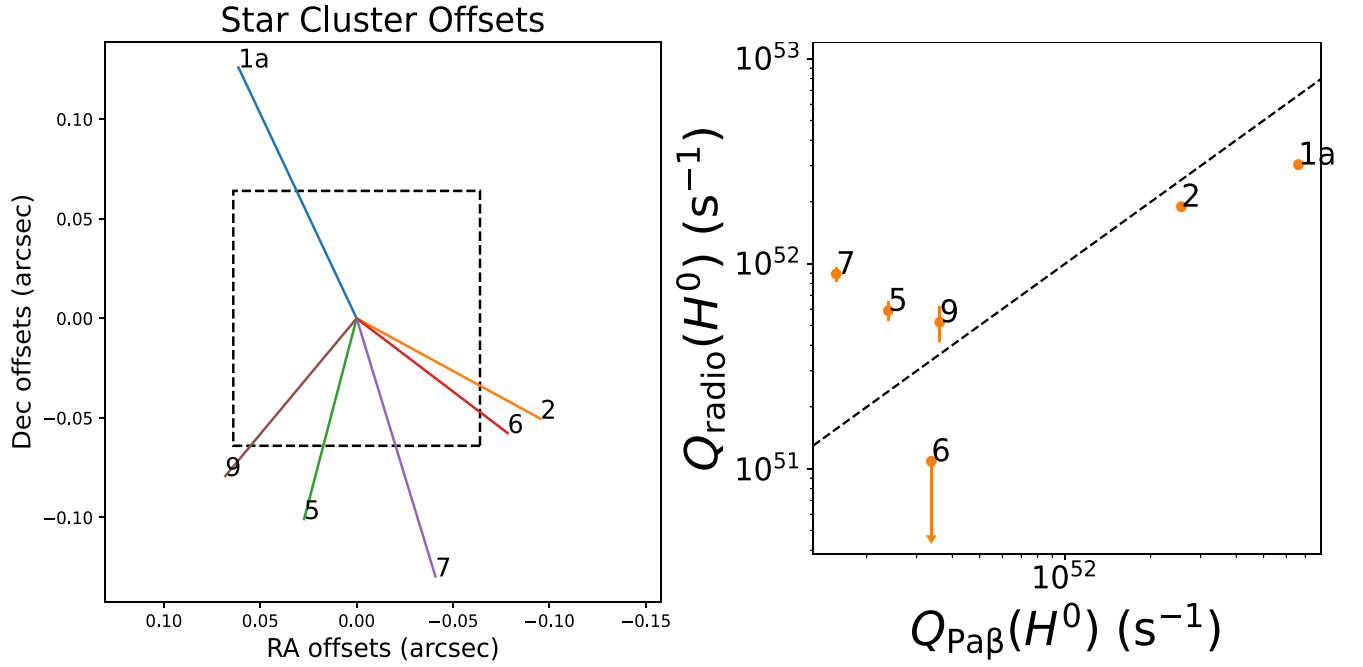


Figure 7. Left: the coordinate offsets between Pa β sources and radio continuum sources. The dashed square shows the pixel size of the Pa β image (0".128). Right: the comparison of the total ionizing photon numbers derived from Pa β and 100 GHz images. The dashed line shows the one-to-one relation.

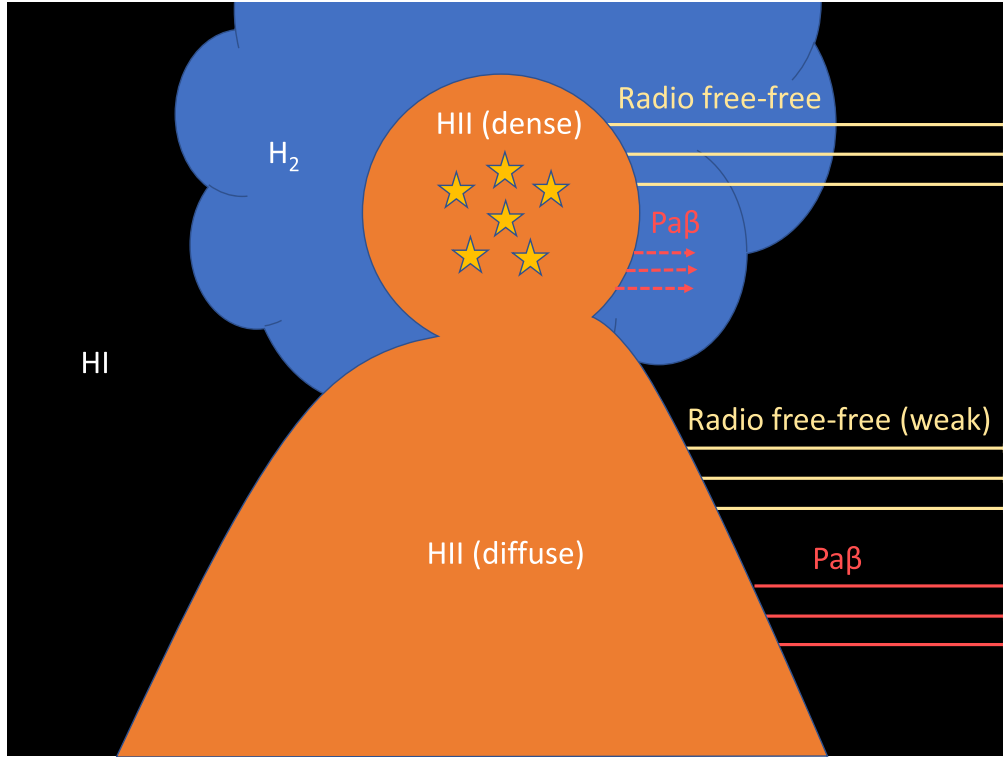


Figure 8. A schematic showing an H II region ionized by a star cluster that is at the edge of the cloud. In addition to the H II region inside the cloud, some photons leak out and ionize some of the H I gas outside of the cloud. The H II region inside the cloud is smaller than the H II region outside the cloud, due to the higher gas pressure in the cloud. Both dense and diffuse H II regions produce radio free-free continuum and Pa β emission. We cannot see the Pa β emission from the H II region inside the cloud due to the high extinction. Outside the cloud, we can see both radio free-free emission and Pa β emission. However, the radio free-free emission might not be detectable due to the low density of the H II region.

4.5. Missing Protostar Cluster: Firecracker

Whitmore et al. (2014) identified a candidate for a protostar cluster called the “Firecracker” in the SMC 2 region. It is luminous and compact in $^{12}\text{CO } J=3-2$, but without any

associate radio counterpart at 3.6 cm (Johnson et al. 2015), which suggests that it is at the very beginning stage of forming stars. Therefore, we do not expect the source to appear in our 100 GHz map. On the other hand, we do expect it to have

Table 5
Measured Properties of Selected GMCs in the Antennae

Index	Coordinates (J2000)	$S_{100\text{GHz}}$ (mJy)	$S_{220\text{GHz,dust}}$ (mJy)	$S_{345\text{GHz,dust}}$ (mJy)	T_{kin} (K)	$\log_{10} M_{\text{gas}}$ (M_{\odot})	$\log_{10} \Sigma_{\text{gas}}$ ($M_{\odot} \text{ pc}^{-2}$)
(1)	(2)	(3)	(4)	(5)	(6)	(7)	(8)
1	12 ^h 01 ^m 54 ^s .96, -18 ^d 53 ^m 05 ^s .86	3.5 ± 0.04	1.5 ± 0.1	6.9 ± 0.5	21.5 ± 0.3	7.86 ± 0.03	3.90 ± 0.03
2	12 ^h 01 ^m 54 ^s .59, -18 ^d 53 ^m 03 ^s .10	1.2 ± 0.03	0.57 ± 0.09	2.6 ± 0.4	12.3 ± 0.4	7.69 ± 0.07	3.85 ± 0.07
3	12 ^h 01 ^m 53 ^s .55, -18 ^d 53 ^m 09 ^s .23	0.25 ± 0.03	0.42 ± 0.08	1.9 ± 0.4	16.8 ± 0.4	7.40 ± 0.09	3.68 ± 0.09
4	12 ^h 01 ^m 53 ^s .51, -18 ^d 53 ^m 10 ^s .26	0.12 ± 0.02	<0.07	<0.3	13.8 ± 0.4	<6.71	<3.17
5	12 ^h 01 ^m 53 ^s .51, -18 ^d 53 ^m 10 ^s .26	0.52 ± 0.03	0.57 ± 0.1	2.6 ± 0.4	22.8 ± 0.3	7.42 ± 0.07	3.55 ± 0.07
6	12 ^h 01 ^m 55 ^s .28, -18 ^d 52 ^m 48 ^s .46	0.21 ± 0.04	0.37 ± 0.1	1.7 ± 0.5	15.8 ± 0.4	7.37 ± 0.13	3.45 ± 0.12
7	12 ^h 01 ^m 55 ^s .46, -18 ^d 52 ^m 45 ^s .65	0.51 ± 0.03	0.71 ± 0.09	3.3 ± 0.4	17.6 ± 0.4	7.61 ± 0.05	3.87 ± 0.05
8	12 ^h 01 ^m 55 ^s .14, -18 ^d 52 ^m 40 ^s .86	0.18 ± 0.03	0.45 ± 0.09	2.1 ± 0.4	14.3 ± 0.4	7.51 ± 0.09	3.70 ± 0.09
9	12 ^h 01 ^m 54 ^s .75, -18 ^d 52 ^m 31 ^s .37	0.19 ± 0.03	0.21 ± 0.08	1.0 ± 0.4	9.9 ± 0.5	7.42 ± 0.16	3.83 ± 0.16
10	12 ^h 01 ^m 52 ^s .13, -18 ^d 52 ^m 20 ^s .76	0.19 ± 0.02	0.24 ± 0.07	1.1 ± 0.3	15.2 ± 0.4	7.21 ± 0.13	3.62 ± 0.13
11	12 ^h 01 ^m 53 ^s .06, -18 ^d 52 ^m 05 ^s .88	0.16 ± 0.03	0.54 ± 0.08	2.5 ± 0.4	19.0 ± 0.3	7.46 ± 0.07	3.76 ± 0.06
12	12 ^h 01 ^m 53 ^s .02, -18 ^d 52 ^m 02 ^s .07	0.46 ± 0.03	1.2 ± 0.1	5.7 ± 0.5	27.5 ± 0.3	7.70 ± 0.04	3.81 ± 0.03
13	12 ^h 01 ^m 54 ^s .58, -18 ^d 51 ^m 56 ^s .55	0.22 ± 0.03	0.43 ± 0.13	2.0 ± 0.6	13.1 ± 0.4	7.55 ± 0.13	3.87 ± 0.13

Note. (1) Source ID. (2) Coordinates. (3) GMC flux at 100 GHz. (4) GMC dust flux at 220 GHz. (5) GMC dust flux at 345 GHz. (6) Peak gas kinetic temperature. (7) GMC gas mass derived from the dust continuum (see Section 5.1). (8) GMC surface density derived from the dust continuum.

strong dust emission at higher frequencies. However, as we see in the 345 GHz map (Figure 1), there is no signal detected in the SGMC 2 region.

Johnson et al. (2015) detected the Firecracker at 345 GHz with a resolution of 0''.5 (53 pc). The peak intensity of the dust continuum reported is $9.8 \times 10^{-4} \text{ Jy beam}^{-1}$. If we assume that it is a perfect point source, the same peak intensity at a 0''.11 resolution would give us an S/N of 25, which is clearly not the case. On the other hand, if we assume that the dust emission is uniformly distributed over the 53 pc area, we would expect an S/N of 1 for the emission peak, which agrees better with what we observe. This analysis clearly suggests that Firecracker has a structure on GMC scales. Furthermore, we would expect the dust temperature to be quite cold throughout the whole area, due to the lack of stellar radiation. Therefore, the dust would not be as luminous as our YMC candidates, and thus the Firecracker would not appear as a strong point source.

5. Comparison with GMC Properties

5.1. Flux at GMC Scales

To measure the fluxes at GMC scales, we apply a similar procedure as that described in Section 3.2, with the aperture determined through a 2D Gaussian fitting to the 100 GHz GMC-scale continuum image. We use a similar procedure to split the free-free emission and dust emission as that described in Section 3.2, although now we are calculating the dust flux at 220 GHz instead of 345 GHz. The free-free emission and the dust emission at 220 GHz are calculated as

$$S_{220\text{GHz,ff}} = S_{100\text{GHz}} \left(\frac{220\text{GHz}}{100\text{GHz}} \right)^{-0.1}; \quad (14)$$

$$S_{220\text{GHz,dust}} = S_{220\text{GHz}} - S_{220\text{GHz,ff}}. \quad (15)$$

Previous studies (e.g., Whitmore et al. 2010) have used continuum data with a ~ 60 pc resolution to study star clusters, which generally have diameters of several pc. This approach will potentially include emission from outside the star cluster. A comparison between our 61 pc and 12 pc resolution data will enable us to quantify this bias. In addition, the ratio between the fluxes from the two spatial scales will tell us how concentrated the star formation is in each individual GMC.

After we split the dust emission from the free-free emission, we can calculate the GMC gas mass based on Equations (6) and (7), with the dust temperature calculated using Equation (5). The GMC properties are summarized in Table 5.

To compare the dust emission at different scales, we need to extrapolate the dust flux at 220 GHz to the flux at 345 GHz. We assume that the dust is still optically thin, so that the graybody dust spectrum is (Casey 2012)

$$S_{\nu,\text{dust}} \propto \frac{\nu^{\beta+3}}{e^{h\nu/kT} - 1} \propto \nu^{\beta+2}, \quad (16)$$

where β is the dust emissivity index and we assume $\beta = 1.5$. The extrapolated flux at 345 GHz can be calculated as

$$S_{345\text{GHz,dust}} = S_{220\text{GHz,dust}} \left(\frac{345\text{GHz}}{220\text{GHz}} \right)^{3.5}. \quad (17)$$

The flux ratios are shown in the left panel of Figure 9. As we can see, the flux ratio for free-free emission is about 50%, while the dust emission fraction is $\sim 20\%$. The free-free emission traces the ionized gas component, which lets us calculate the mass of the stellar component based on the SSP assumption, while the dust emission traces the gas component. Therefore, we can conclude that the stellar component is more concentrated in YMCs than is the gas component. We note that the gas in the YMCs is generally warmer than the gas outside the YMCs (Tables 2 and 5). As indicated by Equation (16), warmer dust is more luminous. Hence, the fraction of central gas over total GMC gas mass may be even lower than the observed luminosity ratio of 20%. These results are consistent with simulations (Li et al. 2019) that show that the stellar component is more radially concentrated than the gas component in GMCs.

Figure 9 also shows that sources 3 and 4 have flux ratios greater than 100%. If we increase the sensitivity of the image by using a robust parameter of 2.0 instead of 0.5, we recover even higher fluxes at YMC scales, which exceed the allowed uncertainty range. Since our GMC-scale map has an LAS of $\sim 70''$, this difference is unlikely to be caused by missing flux at large scales. Because the YMC-resolution data were taken two years before the GMC-resolution data, it is possible that these two sources are time-variable sources with decreasing

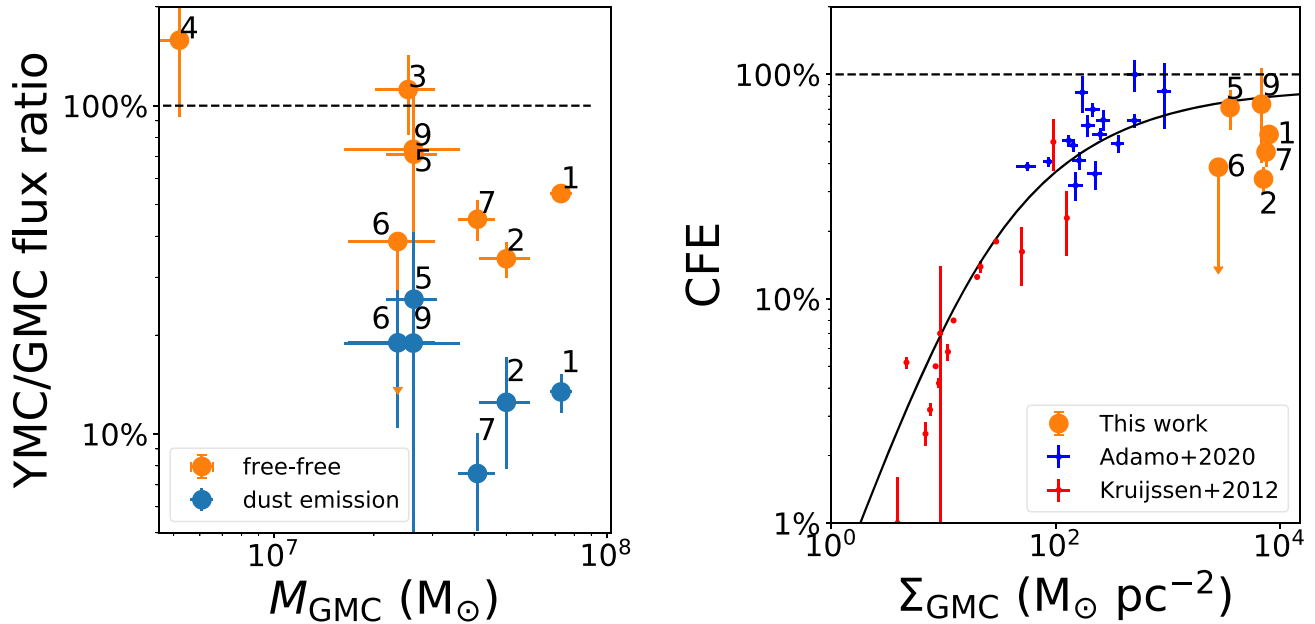


Figure 9. Left: the ratio of the flux at YMC scales to that at GMC scales vs. the GMC mass. Flux ratios are shown for both free-free emission and dust emission. Right: the YMC-to-GMC ratio for free-free emission, which is equivalent to the CFE, vs. the gas surface density. The mean gas surface density for the individual YMCs from the Antennae is taken to be the gas surface density at GMC scales (Table 5). The blue and red points are the CFEs for individual galaxies compiled by Adamo et al. (2020) and Kruijssen (2012). The solid curve is the theoretical prediction of the CFE from Kruijssen (2012). We can see that the CFEs for individual GMCs in the Antennae generally agree with the observations and theoretical predictions for entire galaxies.

luminosity with time. As shown in Figure 1, these two sources are close to the southern nucleus, and so it is possible these sources are active galactic nuclei or supernovae.

5.2. Cluster Formation Efficiency

The ratio of free-free emission at YMC scales compared to GMC scales basically characterizes the fraction of stars formed in bound star clusters, which is equivalent to the cluster formation efficiency (CFE). We ignore the “cruel cradle factor” (Kruijssen 2012), which is the fraction of stars that remain bound after the cloud is dispersed. Kruijssen (2012) derived theoretical predictions for the global CFE of galaxies. Among all the factors, CFEs are most strongly dependent on the mean gas surface density of the galaxy. To compare with this theoretical prediction, we plot our free-free flux ratio versus the GMC surface density in the right panel of Figure 9. The GMC surface density is derived from the dust flux at the 220 GHz continuum. We also overlay the literature data (compiled by Kruijssen 2012; Adamo et al. 2020) for comparison; in these studies, each data point represents a measurement for a single galaxy. We can see that our measurements for individual GMCs are close to but below the theoretical prediction. Since our data points are all at the high gas surface density end, we cannot use our new data on their own to fit the whole trend and see if they agree with the theoretical prediction.

We note that in the model of Kruijssen (2012), both the CFE and the gas surface density are global quantities for each individual galaxy. Here, we are trying to apply this model to GMC scales. The major effect is that the model is averaging gas at much larger scales, and so the gas surface density should be lower than the surface density for individual GMCs, which could bring the data points leftward.

5.3. Mass Correlation between GMCs and YMCs

Clusters generally form in the densest parts of GMCs (Krumholz et al. 2019). As they form, feedback starts to take effect and eventually removes the gas, thereby limiting the star formation efficiency (SFE). It is known from observations that the mass functions of YMCs and GMCs have similar power-law slopes of -2.0 , which suggest a relatively constant SFE (e.g., Mok et al. 2020). However, the statistical cutoff due to the rarity of GMCs and YMCs at the upper mass end makes it hard to study this relation for the massive clouds ($\sim 10^8 M_{\odot}$) that are common in LIRGs and ULIRGs. On the other hand, idealized simulations confirm a tight correlation between the maximal cluster mass and GMC mass (Howard et al. 2018) up to GMC masses of $10^6 M_{\odot}$. Radio observations can probe the most massive YMCs ($\sim 10^6 M_{\odot}$) when they are still associated with clouds, thus enabling us to match these YMCs with their host GMCs.

In Figure 10, we plot the stellar mass and total mass of YMCs versus the GMC molecular gas mass for the Antennae, NGC 253, and the Milky Way. For the Milky Way, the stellar masses of YMCs are from Krumholz et al. (2019). Since most of these YMCs are already outside the host molecular cloud, we assume that the total masses of these clusters are the same as their stellar masses. We then match the Milky Way YMCs with their closest GMCs using the GMC catalog in Rice et al. (2016). We exclude matched clouds where the closest distance is greater than 300 pc. If there are more than two clusters belonging to the same cloud, we only show the cluster with the maximum stellar mass. For NGC 253, the YMC data is from Leroy et al. (2018), while the GMC data is from Leroy et al. (2015). We overlay the YMCs on Figure 9 in Leroy et al. (2015), to spatially match each YMC with its corresponding GMC. We then compare the central velocity of the YMCs with their matched GMCs to confirm this correspondence. If the

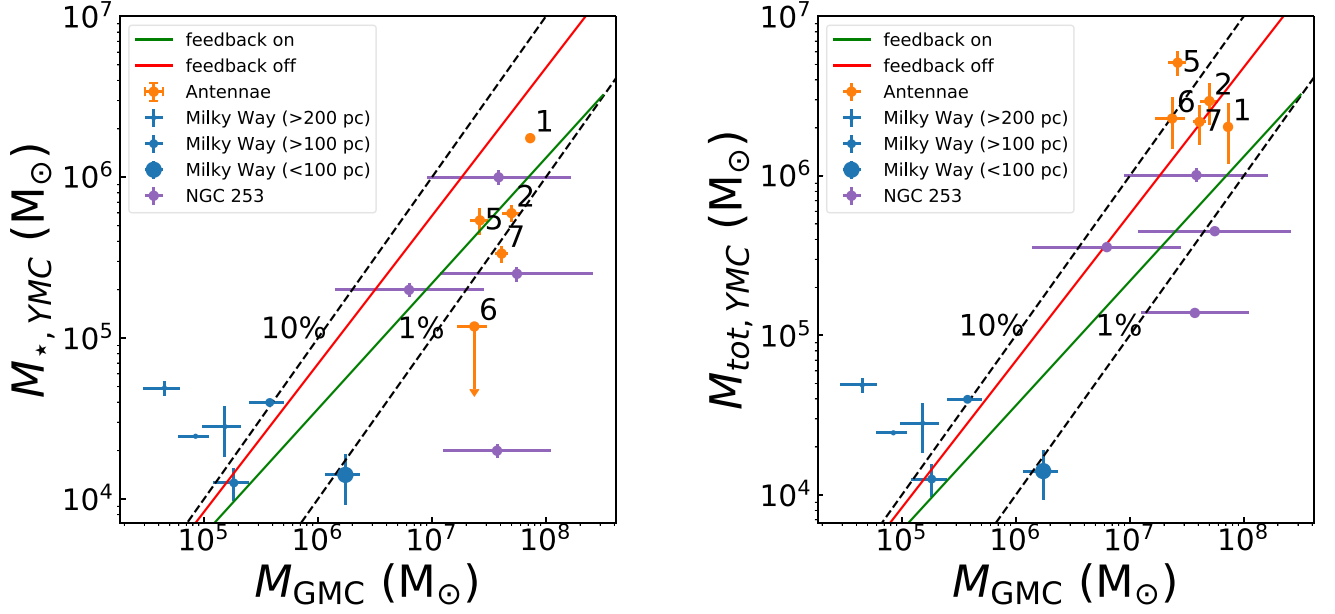


Figure 10. YMC stellar mass (left) and total mass (right) vs. the host GMC mass. The red and green solid lines are simulations from Howard et al. (2018), with feedback off and on. The two dashed lines are constant ratios of 0.1 and 0.01. We can see that the observational data generally agree with the simulation predictions.

central velocity does not match, we find the closest cloud that has a velocity range covering the YMC central velocity. The same rule, that we only show the cluster with maximum stellar or total mass, applies if we have more than one YMC corresponding to a single GMC. We also plot the simulation predictions for the YMC–GMC mass relation from Howard et al. (2018), with feedback on and off. Note that this relation is between the GMC mass and the maximum YMC mass within that GMC. The upper limit of the GMC mass in this simulation is $10^6 M_\odot$, and so we must extrapolate the relation to higher masses of $\sim 10^8 M_\odot$.

From Figure 10, we can see that the data generally agree with the correlations predicted by the simulation. For the Milky Way data points, we use symbols of different sizes to represent the clusters in different distance ranges from their matched GMCs. We can see that the YMCs more than 200 pc away from their matched GMCs are all far above the simulation predictions. Since GMC diameters are generally smaller than 100 pc in the Milky Way (Heyer & Dame 2015), we would expect those YMCs to be outside their matched GMCs. A probable scenario is that those YMCs have already dispersed a significant amount of gas in their host GMCs, and hence their matched GMC mass is less than what we expect. In contrast, the YMC with a distance less than 100 pc from its matched GMC shows a stellar mass less than what we expect. This YMC is probably still embedded in its matched GMC, and may be continuing to form stars.

We can also see that the YMCs in NGC 253 have a similar mass range as the YMCs in the Antennae. For NGC 253, there is one data point significantly below the simulation predictions. We would expect this YMC to be very young and that lots of stars are yet to form. In the right panel of Figure 10, where we plot the total YMC mass versus the GMC gas mass, we can see that the data point is closer to the simulation predictions. YMCs in the Antennae show less scatter in the left panel, and seem to agree better with the feedback-on relation from Howard et al. (2018). However, we note that those values may be lower limits, since some of the YMCs are still going to form stars

(see Section 4.1). If we plot the total mass versus the GMC mass, we can see that those points are clustered around the feedback-off relation. However, as we discussed in Section 4.2, we probably include a lot of gas that is outside of the YMCs. Therefore, the data points in the right panel of Figure 10 should be considered as upper limits. Also, due to our limited sample size and heterogeneous data sources, the results in this section should be considered to be illustrative, and still in need of further investigation.

5.4. No Effect of YMCs on GMC Temperatures

It is interesting to see if clouds with YMCs have different properties from clouds without YMCs. As we know, YMCs have strong free–free emission, which could heat the dust and make the clouds warmer. Therefore, we might expect a temperature difference between clouds with or without YMCs. We apply Equation (5) to the $^{12}\text{CO } J=2-1$ data at GMC resolution (N. Brunetti et al. 2022, in preparation). To avoid effects from correlated pixels, we Nyquist sample the image by rebinning the pixels to half of the beam. Figure 11 shows the calculated T_{kin} versus the surface density of the molecular gas. Note that in this plot, the gas surface density is calculated based on the GMC-resolution $^{12}\text{CO } J=2-1$ cube, since we do not have 220 GHz continuum detections for all $^{12}\text{CO } J=2-1$ detected pixels. The gray points show all the detected pixels in the $^{12}\text{CO } J=2-1$ map with peak brightness temperatures greater than 10 times the rms noise. The orange points are the peak values of the pixels within our apertures used to measure the flux of the continuum point source at GMC scales. Those points represent the properties of the GMCs that host radio YMCs. We also divide the data points into different bins, based on the gas surface density values, and calculate the median for each bin (blue points; the error bars show the values of the first and third quartiles of each bin).

From the plot, we can see that the orange points are generally above the blue points. However, at the high-surface-density end ($5000\text{--}10,000 M_\odot \text{ pc}^{-2}$), three of the four YMCs have

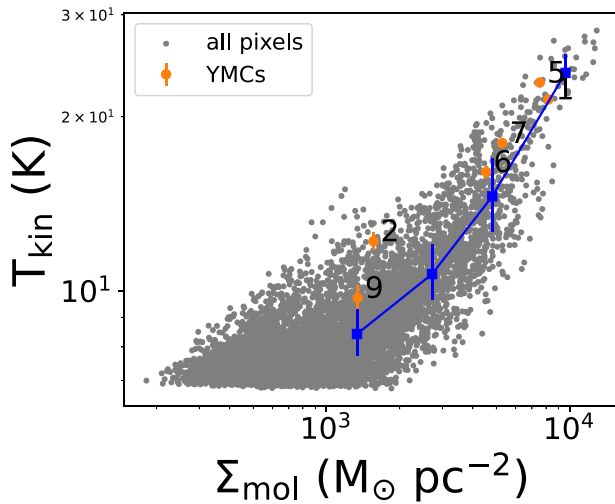


Figure 11. The GMC temperatures derived from CO 2–1 observations at a resolution of ~ 60 pc vs. the molecular gas surface density. We assume a ULIRG α_{CO} of $1.1 M_{\odot} (\text{K km s}^{-1} \text{pc}^2)^{-1}$. The gray points are all pixels detected in the $^{12}\text{CO } J = 2-1$ map. The orange points are pixels in the $^{12}\text{CO } J = 2-1$ map that coincide with peaks of the continuum source. The blue points and error bars represent the median and 25th and 75th percentile values at each given bin for gas surface density. There is no strong evidence that the temperatures of the GMCs that are forming YMCs are significantly higher than the temperatures of the remaining GMCs.

temperatures lower than the first quartile values, which indicates that their temperature is not significantly different from the rest of the pixels. On the other hand, we see that two orange points are above the first quartile values at the low-surface density end ($\sim 1000 M_{\odot} \text{pc}^{-2}$). However, in this surface density regime, we are hitting the sensitivity limit of the 100 GHz YMC-resolution continuum. Source 9 is barely detected in our high-resolution continuum image, so we can consider it to mark the lower detection limit. Therefore, our methods of identifying YMCs bias toward sources with high peak brightness temperatures at low-mass surface densities. Overall, we see no clear evidence that the feedback from the YMCs has increased the temperature of the host GMCs yet. However, since we only have a limited number of radio sources, our results cannot conclusively show whether YMC feedback has affected the GMCs yet. In the future, we will consider adding young optical star clusters to this type of analysis.

6. Conclusions

In this paper, we have presented new, high-resolution continuum data for YMCs in the Antennae. We combine these data with CO and continuum data at GMC scales to explore the correlation of properties between the YMCs and their host GMCs. Our main conclusions are summarized below.

1. These YMCs have stellar masses of $\sim 10^5$ – $10^6 M_{\odot}$ and radii of ~ 3 – 15 pc. For sources 1b, 2, and 5, we can observe substructures in higher-resolution images, which suggests that we might overestimate their radii by including some surrounding diffuse emission. Sources 1a and 7 still look compact at the highest resolution.
2. Based on statistical counts, we estimate the lifespans of these YMCs to be about 1 Myr. This is consistent with estimates of embedded YMC lifetimes. However, all

these sources have $\text{Pa}\beta$ counterparts. By comparing the coordinates and fluxes between 100 GHz and $\text{Pa}\beta$ sources, we think that these YMCs have partly emerged and have already ionized some diffuse medium outside the cloud.

3. A virial analysis of these YMCs suggests that the majority are bound systems. This further suggests that they may appear as young globular clusters after the gas is dispersed.
4. More than 50% of the free-free emission at GMC scales comes from compact YMCs inside those GMCs. This fraction is equivalent to the CFE. We compare this fraction with the theoretical prediction from Kruijssen (2012) and literature data for the galaxies from Adamo et al. (2020), and see a quite good agreement.
5. We explore the correlation between the YMC mass and its host GMC mass. We also compare this correlation in the Antennae with those in NGC 253 and the Milky Way. We find that the data generally agree with the predicted correlation from the simulations (Howard et al. 2018).
6. When comparing the gas temperatures in regions with and without YMCs, we find no significant difference between those two populations of clouds. We see no clear evidence that YMC feedback has increased the cloud temperature at GMC scales.

We thank the referee for thoughtful comments and constructive suggestions. This paper makes use of the following ALMA data: ADS/JAO.ALMA #2016.1.00041.S, ADS/JAO.ALMA #2016.1.00924.S, and ADS/JAO.ALMA #2018.1.00272.S. ALMA is a partnership of ESO (representing its member states), NSF (USA), and NINS (Japan), together with NRC (Canada), MOST and ASIAA (Taiwan), and KASI (Republic of Korea), in cooperation with the Republic of Chile. The Joint ALMA Observatory is operated by ESO, AUI/NRAO, and NAOJ. The National Radio Astronomy Observatory is a facility of the National Science Foundation operated under cooperative agreement by Associated Universities, Inc. This research has made use of NASA’s Astrophysics Data System Bibliographic Services. This research has made use of Astropy,⁵ a community-developed core Python package for Astronomy (Astropy Collaboration et al. 2013, 2018). The research of C.D.W. is supported by grants from the Natural Sciences and Engineering Research Council of Canada and the Canada Research Chairs program. The research of H.H. is partially supported by the New Technologies for Canadian Observatories, an NSERC-CREATE training program. The research of K.J. is supported by NSF grant No. 1716335.

Facility: ALMA .

Software: astropy (Astropy Collaboration et al. 2013, 2018), CASA (McMullin et al. 2007).

ORCID iDs

Hao He <https://orcid.org/0000-0001-9020-1858>
 Christine Wilson <https://orcid.org/0000-0001-5817-0991>
 Nathan Brunetti <https://orcid.org/0000-0002-0154-7724>
 Molly Finn <https://orcid.org/0000-0001-9338-2594>
 Ashley Bemis <https://orcid.org/0000-0003-0618-8473>
 Kelsey Johnson <https://orcid.org/0000-0001-8348-2671>

⁵ <http://www.astropy.org>

References

- Adamo, A., Hollyhead, K., Messa, M., et al. 2020, *MNRAS*, **499**, 3267
- Astropy Collaboration, Price-Whelan, A. M., Sipőcz, B. M., et al. 2018, *AJ*, **156**, 123
- Astropy Collaboration, Robitaille, T. P., Tollerud, E. J., et al. 2013, *A&A*, **558**, A33
- Bolatto, A. D., Wolfire, M., & Leroy, A. K. 2013, *ARA&A*, **51**, 207
- Brogan, C., Johnson, K., & Darling, J. 2010, *ApJL*, **716**, L51
- Brown, G., & Gnedin, O. Y. 2021, *MNRAS*, **508**, 5935
- Calzetti, D., Armus, L., Bohlin, R. C., et al. 2000, *ApJ*, **533**, 682
- Casey, C. M. 2012, *MNRAS*, **425**, 3094
- Chevance, M., Kruijssen, J. M. D., Vazquez-Semadeni, E., et al. 2020, *SSRv*, **216**, 50
- Cleri, N. J., Trump, J., Backhaus, B. E., et al. 2020, arXiv:2009.00617
- Costa, A. H., Johnson, K. E., Indebetouw, R., et al. 2021, *ApJ*, **918**, 76
- Draine, B. T. 2003, *ARA&A*, **41**, 241
- Emig, K. L., Bolatto, A. D., Leroy, A. K., et al. 2020, *ApJ*, **903**, 50
- Fall, S. M., & Zhang, Q. 2001, *ApJ*, **561**, 751
- Finn, M. K., Johnson, K. E., Brogan, C. L., et al. 2019, *ApJ*, **874**, 120
- Gilbert, A. M., & Graham, J. R. 2007, *ApJ*, **668**, 168
- Ginsburg, A., Goss, W. M., Goddi, C., et al. 2016, *A&A*, **595**, A27
- Grasha, K., Calzetti, D., Bittler, L., et al. 2018, *MNRAS*, **481**, 1016
- Hannon, S., Lee, J. C., Whitmore, B. C., et al. 2019, *MNRAS*, **490**, 4648
- Harris, W. E., Harris, G. L. H., & Alessi, M. 2013, *ApJ*, **772**, 82
- Heyer, M., & Dame, T. M. 2015, *ARA&A*, **53**, 583
- Hollyhead, K., Bastian, N., Adamo, A., et al. 2015, *MNRAS*, **449**, 1106
- Howard, C. S., Pudritz, R. E., & Harris, W. E. 2018, *NatAs*, **2**, 725
- Israel, F. P. 1978, *A&A*, **70**, 769
- Johnson, K. E., Hunt, L. K., & Reines, A. E. 2009, *AJ*, **137**, 3788
- Johnson, K. E., Indebetouw, R., Watson, C., & Kobulnicky, H. A. 2004, *AJ*, **128**, 610
- Johnson, K. E., & Kobulnicky, H. A. 2003, *ApJ*, **597**, 923
- Johnson, K. E., Leroy, A. K., Indebetouw, R., et al. 2015, *ApJ*, **806**, 35
- Kepley, A. A., Tsutsumi, T., Brogan, C. L., et al. 2020, *PASP*, **132**, 024505
- Kessler, S., Leroy, A., Querejeta, M., et al. 2020, *ApJ*, **892**, 23
- Klaas, U., Nielbock, M., Haas, M., Krause, O., & Schreiber, J. 2010, *A&A*, **518**, L44
- Kobulnicky, H. A., & Johnson, K. E. 1999, *ApJ*, **527**, 154
- Kruijssen, J. M. D. 2012, *MNRAS*, **426**, 3008
- Krumholz, M. R., McKee, C. F., & Bland-Hawthorn, J. 2019, *ARA&A*, **57**, 227
- Leroy, A. K., Bolatto, A. D., Ostriker, E. C., et al. 2015, *ApJ*, **801**, 25
- Leroy, A. K., Bolatto, A. D., Ostriker, E. C., et al. 2018, *ApJ*, **869**, 126
- Leroy, A. K., Hughes, A., Liu, D., et al. 2021, *ApJS*, **255**, 19
- Levy, R. C., Bolatto, A. D., Leroy, A. K., et al. 2021, *ApJ*, **912**, 4
- Li, H., & Gnedin, O. Y. 2014, *ApJ*, **796**, 10
- Li, H., Vogelsberger, M., Marinacci, F., & Gnedin, O. Y. 2019, *MNRAS*, **487**, 364
- Matthews, A. M., Johnson, K. E., Whitmore, B. C., et al. 2018, *ApJ*, **862**, 147
- McCraday, N., & Graham, J. R. 2007, *ApJ*, **663**, 844
- McKee, C. F., & Ostriker, E. C. 2007, *ARA&A*, **45**, 565
- McMullin, J. P., Waters, B., Schiebel, D., Young, W., & Golap, K. 2007, in ASP Conf. Ser., 376, Astronomical Data Analysis Software and Systems XVI, ed. R. A. Shaw, F. Hill, & D. J. Bell (San Francisco, CA: ASP), **127**
- Mok, A., Chandar, R., & Fall, S. M. 2020, *ApJ*, **893**, 135
- Murphy, E. J., Condon, J. J., Schinnerer, E., et al. 2011, *ApJ*, **737**, 67
- Neff, S. G., & Ulvestad, J. S. 2000, *AJ*, **120**, 670
- Osterbrock, D. E. 1989, *Astrophysics of Gaseous Nebulae and Active Galactic Nuclei* (Sausalito, CA: University Science)
- Reines, A. E., Johnson, K. E., & Goss, W. M. 2008, *AJ*, **135**, 2222
- Rice, T. S., Goodman, A. A., Bergin, E. A., Beaumont, C., & Dame, T. M. 2016, *ApJ*, **822**, 52
- Rico-Villas, F., Martín-Pintado, J., González-Alfonso, E., Martín, S., & Rivilla, V. M. 2020, *MNRAS*, **491**, 4573
- Schirm, M. R. P., Wilson, C. D., Madden, S. C., & Clements, D. L. 2016, *ApJ*, **823**, 87
- Schweizer, F., Burns, C. R., Madore, B. F., et al. 2008, *AJ*, **136**, 1482
- Scoville, N. Z., Evans, A. S., Thompson, R., et al. 2000, *AJ*, **119**, 991
- Scoville, N. Z., Polletta, M., Ewald, S., et al. 2001, *AJ*, **122**, 3017
- Stanford, S. A., Sargent, A. I., Sanders, D. B., & Scoville, N. Z. 1990, *ApJ*, **349**, 492
- Tsuge, K., Sano, H., Tachihara, K., et al. 2019, *ApJ*, **871**, 44
- Whitmore, B. C., Brogan, C., Chandar, R., et al. 2014, *ApJ*, **795**, 156
- Whitmore, B. C., Chandar, R., & Fall, S. M. 2007, *AJ*, **133**, 1067
- Whitmore, B. C., Chandar, R., Schweizer, F., et al. 2010, *AJ*, **140**, 75
- Whitmore, B. C., & Zhang, Q. 2002, *AJ*, **124**, 1418
- Whitmore, B. C., Zhang, Q., Leitherer, C., et al. 1999, *AJ*, **118**, 1551
- Wilson, C. D., Harris, W. E., Longden, R., & Scoville, N. Z. 2006, *ApJ*, **641**, 763
- Wilson, C. D., Petitpas, G. R., Iono, D., et al. 2008, *ApJS*, **178**, 189
- Wilson, C. D., Scoville, N., Madden, S. C., & Charmandaris, V. 2000, *ApJ*, **542**, 120
- Wilson, C. D., Scoville, N., Madden, S. C., & Charmandaris, V. 2003, *ApJ*, **599**, 1049
- Zhang, Q., Fall, S. M., & Whitmore, B. C. 2001, *ApJ*, **561**, 727